Paper 2:

Ion velocity distributions in the sheath and presheath of a biased object in plasma

W. J. Miloch, N. Gulbrandsen, L. N. Mishra, and Å. Fredriksen, *Physics of Plasmas*, **18**, 083502, (2011), doi: 10.1063/1.3614520.

Ion velocity distributions in the sheath and presheath of a biased object in plasma

W. J. Miloch, N. Gulbrandsen, L. N. Mishra, and Å. Fredriksen
Department of Physics and Technology, University of Tromsø, 9037 Tromsø, Norway

(Received 11 April 2011; accepted 29 June 2011; published online 5 August 2011)

Ion velocity distributions in the vicinity of a spherical object with a negative potential with respect to collisionless, source-free plasma are studied with three-dimensional numerical simulations. The ion dynamics around the object leads to distorted radial velocity distributions in the presheath and the sheath edge region. Far in the sheath, an increase in the thermal velocity in the radial direction is observed. Different potentials of the object, ion temperatures, and ion masses are considered, as well as the role of spatial and temporal resolutions in laboratory measurements of ion velocity distributions. The simulations are carried out with the DiP3D, a three-dimensional particle-in-cell numerical code. © *2011 American Institute of Physics*. [doi:10.1063/1.3614520]

I. INTRODUCTION

A region of disturbed plasma density, so-called *sheath* forms in a vicinity of any object being in contact with plasma, if the electric potential of the object is different than that of the plasma.[1] Without external bias, the object will be at floating potential, at which the electron and ion currents balance each other. In electropositive plasmas, the floating potential will be negative with respect to the plasma potential. Examples of objects at floating potentials are spacecrafts or meteoroids in space, or dust grains in plasma processing devices.[2] Often, plasma is in contact with biased or grounded surfaces, such as probes or substrates. The sheath in the vicinity of a biased object can be larger than for a floating object.

The sheath modifies plasma conditions locally. A proper understanding of the plasma-object interactions, and in particular the influence of the object on the plasma particle distributions in its vicinity, is crucial for plasma diagnostics and processing. In this paper, we present for the first time results from the three-dimensional particle-in-cell (PIC) simulations for studies of ion velocity distribution function (ivdf) in the sheath of a spherical object in stationary and flowing plasmas with no plasma sources.

For the sheath to exist, the ion speed at the sheath edge must satisfy the Bohm condition, which was originally derived for cold ions[3] and was later generalized for arbitrary ion distributions.[4–6] To satisfy this condition, ions need to be accelerated in a quasi-neutral region, a *presheath*. In the cold ion approximation, the potential drop associated with the presheath relates to the electron temperature: $\Delta\Phi = kT_e/2$.[7] One-dimensional analytical models of the plasma-wall transition for non-zero ion temperatures show that the ivdf will change in the presheath, while in the sheath, ivdf will get narrower[8,9] or broader due to collisions enhanced by instabilities.[6] The models by Emmert *et al.*[8] and by Bissel and Johnson[9] assume different ion source functions, the flux, and Maxwellian source distribution functions, respectively, which result in different ivdf at the sheath edge.[10] In the limit of low ion temperature, both models give asymmetric ivdf with an enhancement at lower velocities.[11,12] Some of these results were supported by one-dimensional particle-in-cell and hybrid numerical simulations.[10,12–15]

The understanding of ion velocity distributions in the plasma-wall transition region is crucial for plasma processing and diagnostics.[16] Both substrates and diagnostic tools are often at large negative bias with respect to the plasma potential and they can significantly modify ivdf. Thus, recently an increased effort has been made in experimental studies of ivdfs close to planar surfaces using the laser induced fluorescence (LIF) technique.[17–21] The experiments showed distorted ivdfs in the presheath, but some results also showed broadening of ivdfs in the sheath.[20] Large distortions of ivdfs close to the electrode have recently been measured using LIF for plasmas in a RF frequency discharge.[22]

In many plasmas of interest, the plasma source is spatially limited, and the production in the presheath and sheath can be neglected. This is valid for tenuous plasmas and objects placed far from the plasma source, such as satellites, or probes in expanding plasmas or edge regions. One-dimensional analytical and numerical models do not consider a source-free plasma.[8–10,12,13] Moreover, one-dimensionality implies plasma interactions with infinite walls. Thus, to study ivdfs in the vicinity of a finite-sized object, three-dimensional plasma dynamics should be considered. The problem is more intricate for objects exposed to a plasma flow.[23,24] Such studies are crucial for interpretation of data from satellite and laboratory measurements. As a detailed analytical and experimental study of the problem is difficult, one can consider using numerical simulations, which allow for self-consistent studies of complex nonlinear systems. We investigate ivdfs in the vicinity of a biased, spherical object in both stationary and flowing plasmas using three-dimensional PIC numerical simulations.

II. NUMERICAL CODE

In the PIC method, the trajectories of plasma particles are followed in self-consistent electric fields. The PIC method uses the grid for reducing the complexity of the numerical algorithm.[25] Without the grid, the net force acting on

each individual plasma particle would need to be calculated in each time step from the interactions with all other particles in the simulation domain. Thus, the complexity of the algorithm would be $\mathcal{O}(n^2)$, where n is the number of simulated particles and $\mathcal{O}$ relates to the computer resources usage time, and the algorithm will resemble the molecular dynamics method. In PIC codes, the particle quantities, such as charge or velocity, are weighted to the grid points, and the corresponding densities are built on the grid. In each time step, the fields and forces are calculated on the grid. The forces are then projected from grid points to the plasma particles in the neighboring grid cells, and the particle trajectories are advanced. The complexity of the PIC algorithm is usually $\mathcal{O}(n) + \mathcal{O}(n_g \log(n_g))$, where n_g is the number of grid points, with $n_g \ll n$, and $\mathcal{O}(n_g \log(n_g))$ is the complexity of solving the field equations. Thus, PIC simulations with a large number of plasma particles are much faster than molecular dynamics simulations, and they allow for studies of kinetic plasma phenomena over periods of time much larger than characteristic time associated with plasma, such as electron or ion plasma periods.

For our simulations, we use the DiP3D code, which was described in detail in previous works,[26,27] and, thus, we specify here only the plasma parameters used for the present study. As a reference case, we simulate argon plasma with density $n = 2.5 \times 10^{16}$ m^{-3}, and real ion mass $m_i = 6.64 \times 10^{-26}$ kg. The plasma is collisionless, i.e., we do not consider any explicit collisions. Far from the object, electrons and ions have Maxwellian velocity distributions, with the electron temperature $T_e = 4$ eV and electron to ion temperature ratio $\gamma = T_e/T_i = 10$. A conducting sphere of diameter $d = 9.2\lambda_{\mathrm{De}} = 30.5\lambda_{\mathrm{D}}$, where $\lambda_{\mathrm{De}} = \sqrt{\varepsilon_0 k_B T_e/(n_e q_e)}$ is the electron Debye length and λ_{D} is the total Debye length defined as $\lambda_{\mathrm{D}}^{-2} = \lambda_{\mathrm{De}}^{-1} + \lambda_{\mathrm{Di}}^{-2}$, is placed inside the simulation box of size $L = 42.1\lambda_{\mathrm{De}}$. The potential of the sphere is set to $\Phi_s = -95$ V with respect to the plasma potential $\Phi_{pl} = 0$ V. This value is approximately five times the floating potential, $\Phi_{fl} = -18$ V, which we find for considered plasma parameters.

In addition to the reference case, we performed a systematic study of the ivdf for different potentials Φ_s of the object, electron to ion temperature ratios γ, and reduced ion mass $m = \nu m_i$, where ν is the reduction factor. The effect of a plasma flow on the ivdf is also considered for flow velocities $v_d = 0.75C_s$ and $v_d = 1.5C_s$. Since changing T_i implies modifying λ_{D}, for presentation of our results, we normalize lengths with λ_{De}. Velocities are normalized with the ion sound speed, chosen as $C_s = \sqrt{kT_e/m}$, where m stands for ion mass.

III. RESULTS

The measured ivdfs are space and time averaged. The time average is taken over three ion plasma periods. For plasmas without the flow, the spatial average is over a sphere for radial distances within the segment $r \in (r_i, r_i + \delta r)$, where r_i is a discretized radial distance from the sphere surface, and $\delta r = r_{i+1} - r_i$. Thus for small r, an increased noise level due to less number of plasma particles is expected. For flowing plasmas, the flow is in the positive x direction, and the spatial average is over a small volume centered at $(x_i, L/2, L/2)$, where L is the size of the simulation box.

Fig. 1 shows ivdfs for radial and azimuthal components of the velocity at different radial distances r from the sphere surface for our reference case as well as the corresponding potential. In the figure, results for two different δr for the radial velocity component are presented: $\delta r = 1.7\lambda_{\mathrm{De}}$ and $\delta r = 0.084\lambda_{\mathrm{De}}$. The radial ivdf is symmetric and close to Maxwellian far away from the sheath edge, which we refer to the potential drop of $\Delta\Phi = kT_e/2 = 2$ eV at $r_s = 9\lambda_{De}$. Already in the presheath, the radial ivdf is shifted towards higher energies and distorted at lower velocities. This distortion at lower velocities in the radial ivdf gets pronounced at the sheath edge, and while entering the sheath, a hump in the distribution forms at lower velocities. The hump diminishes further inside the sheath and contributes to the tail at low velocities, while the radial ivdf is shifted towards higher velocities. For $\delta r = 1.7\lambda_{\mathrm{De}}$, the radial distribution gets wider and distorted further inside the sheath. For $\delta r = 0.084\lambda_{\mathrm{De}}$, the distribution first gets narrower with a steeper slope at

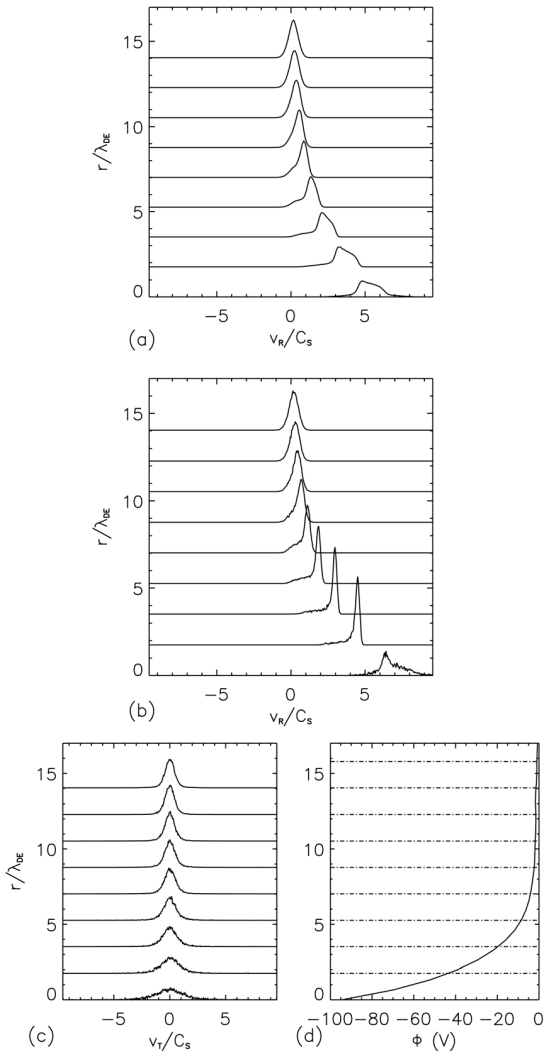

FIG. 1. Normalized radial ivdf for $\delta r = 1.7\lambda_{\mathrm{De}}$ (a), and $\delta r = 0.084\lambda_{\mathrm{De}}$ (b), and azimuthal ivdf for $\delta r = 0.084\lambda_{\mathrm{De}}$ (c) for different distances from the object surface, and the corresponding radial potential Φ (d) for the reference case. The plasma potential is set to zero.

higher velocities and it gets distorted closest to the surface. We note that we find this trend also for $\delta r < 0.084\lambda_{De}$ (these results are not shown in Fig. 1). The azimuthal component, shown in Fig. 1(c), is symmetric for all r, and it is broadened further inside the sheath.

For large spatial averaging in the direction normal to the surface, $\delta r = 1.7\lambda_{De}$, the radial ivdf is distorted and widened in the sheath. This widening increases with decreasing distance to the sphere surface, see Fig. 1(a), and is not present for $\delta r = 0.084\lambda_{De}$ and smaller, except for the last five or six profiles closest to the object. We identify it as a result of superposition of different ivdfs for large δr in the region with the high velocity gradient. Therefore, we use $\delta r = 0.084\lambda_{De}$ in the following.

To quantify the changes in the ivdf in the plasma wall transition region, we measured its full width at half maximum (*fwhm*) and calculated thermal velocity as a measure of temperature from the 2nd central moment of the distribution for $\delta r = 0.084\lambda_{De}$. The 2nd central moment of ivdf is calculated as

$$\left\langle (v_r - \langle v_r \rangle)^2 \right\rangle = \frac{\sum (v_r - \langle v_r \rangle)^2 f(v_r)}{\sum f(v_r)}, \qquad (1)$$

where the sum is due to discrete nature of the distribution $f(v_r)$ from numerical simulations and $\langle v_r \rangle$ is the first raw moment $\langle v_r \rangle = \sum v_r f(v_r) / \sum f(v_r)$. We relate the moments of the ivdf to physical quantities. The first raw moment gives the mean velocity and 2nd central moment gives the variance σ^2, which is proportional to thermal energy. Thermal velocity is calculated as a standard deviation $v_{th} = \sigma$. The results are presented in Fig. 2 as a function of the local potential Φ for the presheath and sheath, up to a few last data points closest to the surface. In addition to our reference case for $\Phi_s = -95$ V, we also present results for $\Phi_s = -45$ V, and $\Phi_s = -18$ V and the corresponding data for distribution according to the Emmert model.[8] For distributions from our simulations, the *fwhm* decreases at the sheath edge reaching approximately half the value of a undisturbed distribution. By comparing the results for *fwhm* for $\Phi_s = -95$ V and $\Phi_s = -40$ V in Fig. 2(a), the increase in the *fwhm* appears to be more dependent on the distance to the object than the local potential. The mean velocity $\langle v_r \rangle$ closely follows the position of the peak of the ivdf, and they both closely follow the total potential drop in the sheath. The thermal velocity v_{th}, which we derive from the variance of the distribution, increases in the beginning of the sheath, with the increase being larger for $\Phi_s = -95$ V than for $\Phi_s = -40$ V. For $\Phi_s = -18$ V, no increase is observed, but instead v_{th} decreases in the sheath. In the presheath, the distribution becomes asymmetric (giving negative skewness, not shown in Fig. 2) forming a low energy tail, and it stays asymmetric throughout the sheath. The forming of the tail can be seen in the increasing thermal velocity around the sheath edge in Fig. 2(c).

We use the analytical solution to Emmert model as a comparison to our results. This solution is only valid in the presheath. To calculate the distribution from the sheath edge and throughout the sheath, we use the energy conservation per particle and assume no source or particle interaction in the sheath, as described in Emmert *et al.*[8] The results for the Emmert model, which are shown for comparison in Fig. 2, differ from our simulations. According to the Emmert model the *fwhm* decreases much more rapidly in the presheath and then continues to decrease throughout the sheath. While the mean velocity also closely follows the potential, thermal velocity increases slightly in the presheath and decreases rapidly at the sheath edge.

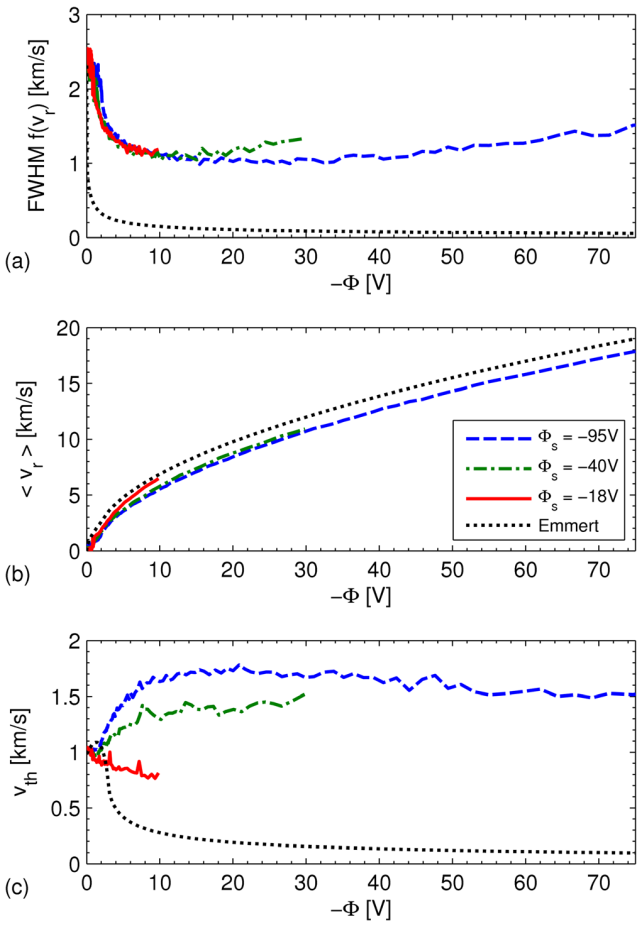

FIG. 2. (Color online) The full width at half maximum, *fwhm* (a), mean velocity $\langle v \rangle$ (b), and thermal velocity v_{th} (c) of the ivdf as a function of the local potential $-\Phi$ for different potentials of the object $\Phi_s = -95$ V, $\Phi_s = -40$ V, and $\Phi_s = -18$ V. The results closest to the surface are not shown as they suffer from statistical noise. The corresponding quantities for the Emmert model are plotted for comparison.

In Fig. 3(a), the radial ivdfs in the presheath, at the sheath edge, and in the middle of the sheath are shown for different temperature ratios γ for $\Phi_s = -95$ V. The distortion in the ivdf shape at the sheath edge is more pronounced for large γ, i.e., colder ions. In the simulations for $\gamma = 100$, the distortion gives rise to a pronounced hump in the radial ivdf at the sheath edge. The distortion gets smaller deeper into the sheath, with the decrease being stronger for colder ions.

The shape of the radial ivdf in the sheath does not change much with the object potential Φ_s, apart from being shifted to higher velocities for more negative local potential in the sheath Φ. In Fig. 3(b), we show results for $\gamma = 10$ at the sheath edge (pos. 2) and in the middle of the sheath, $\Phi = \Phi_s/2$ (pos. 3). In the presheath and at the sheath edge, the ivdf depends on Φ, with the distortion at lower velocities

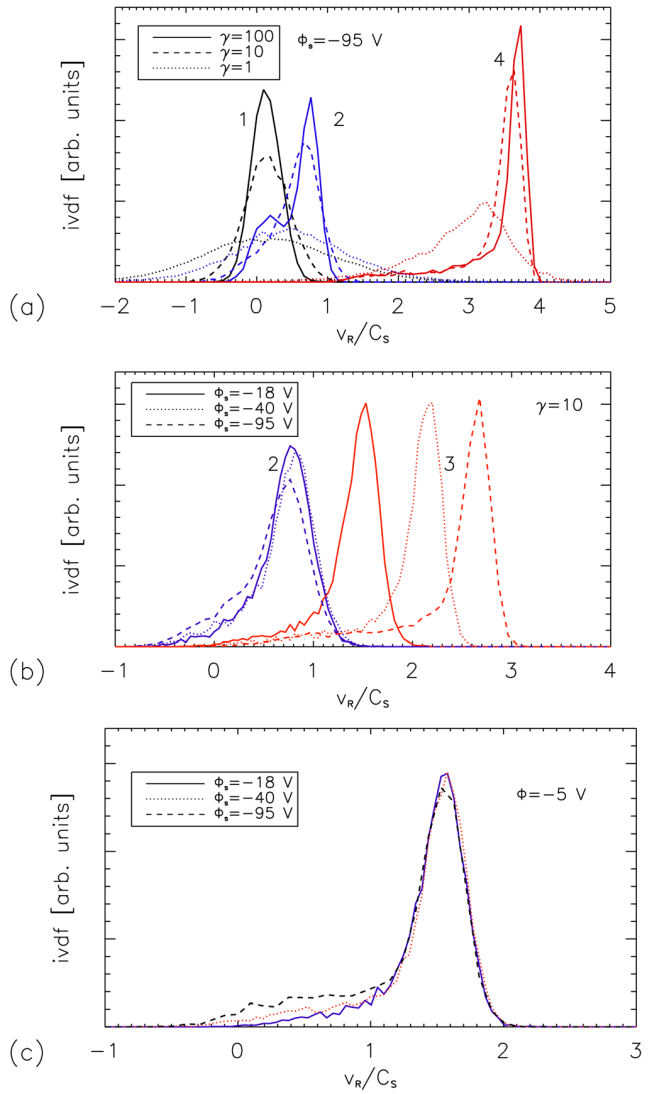

FIG. 3. (Color online) (a) ivdf for different electron to ion temperature ratios γ and $\Phi_s = -95$ V in the presheath $r = 15\lambda_{De}$ (1), sheath edge $r = 9\lambda_{De}$ (2), and in the sheath $r = 3\lambda_{De}$ (4). (b) ivdf at the sheath edge (2) and in the middle of the sheath (4; data taken at $r = r_s/2$, where r_s is a distance corresponding to $\Delta\Phi = kT_e/2$) for different potentials of the object Φ_s for $\gamma = 10$. (c) ivdf for different potentials of the object Φ_s for $\gamma = 10$ in the sheath for the position corresponding to the local potential $\Phi = -5$ V. The heights of the distributions are adjusted to show the relative contribution of the tail at lower velocities. In the online version, different positions are also distinguished by different colors.

being more pronounced for more negative Φ_s. Fig. 3(c) shows distributions in the sheath at $\Phi = -5$ V for different Φ_s. The height of the distributions is normalized for comparison. For larger Φ_s, we see an enhancement in the relative contribution of the slow ion tail. For all Φ_s, there is a finite number of particles with zero velocities.

In Fig. 4, we show the ivdf results from simulations for different m at the same temperature for the sheath edge (pos. 2) and in the sheath (pos. 3). We observe that the hump/tail in the ivdf at the sheath edge is smaller for reduced m, while the shape of the peak of the distribution does not change much with m.

Finally, we performed simulations for flowing plasmas and measured ivdfs for sub- and supersonic velocities, see

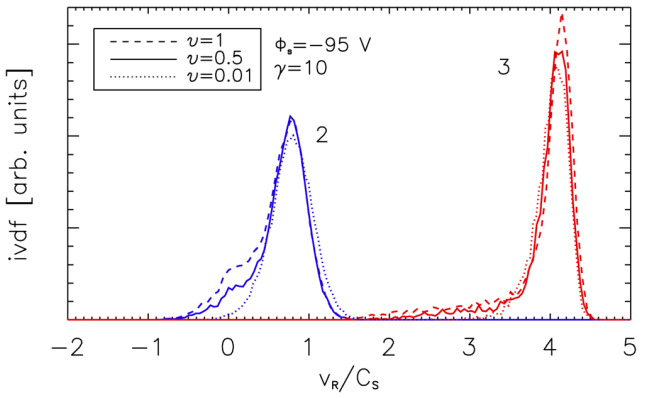

FIG. 4. (Color online) ivdf for reduced ion masses $m = \nu m_i$, where ν is the reduction factor, at the sheath edge $r = 9\lambda_{De}$ (2) and in the sheath $r = 3\lambda_{De}$ (3). $\Phi_s = -95$ V and $\gamma = 10$.

Fig. 5. For supersonic flows ($v_d = 1.5C_s$), we do not observe significant changes in the ivdf in the sheath on the upstream side. For subsonic velocities ($v_d = 0.75C_s$), the ivdf is shifted in the sheath towards supersonic velocities. For both sub- and supersonic flows, the shape of the ivdf at the sheath edge on the downstream side resembles the case for stationary plasma. At the downstream side, ivdfs are broadened in the sheath and distorted at lower velocities, see Fig. 5(b).

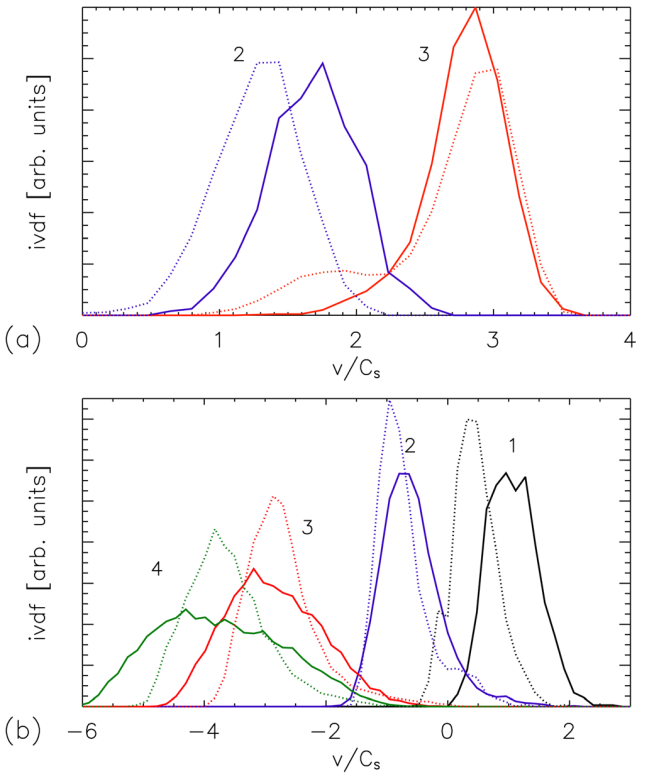

FIG. 5. (Color online) (a) ivdf on the upstream side of the sphere for subsonic (dotted line) and supersonic (solid line) plasma flow at the sheath edge (2), and in the middle of the sheath (3), (b) ivdf on the downstream side of the sphere for subsonic (dotted line) and supersonic (solid line) plasma flow far in the presheath (1), at the sheath edge (2), in the sheath (3), and in the sheath close to the surface (4). The positions at which the ivdf was taken in the sheath on the downstream side are slightly different for sub- and supersonic velocities. Note that in (b) the ions in the sheath have negative velocities.

IV. DISCUSSION

The ivdf is changed in the sheath and presheath of a spherical object at a negative potential with respect to the plasma potential. Already in the presheath, ions are being accelerated towards the object to satisfy the Bohm criterion at the sheath edge. The radial component of the ivdf gets distorted in the presheath, and its evolution in the sheath depends on the plasma parameters and potential drop. Close to the surface of the object, the geometrical effects are also visible.

The distortions of the ivdf at the sheath edge result in a hump/tail at lower velocities, while the width of the distribution is approximately half of the value for the undisturbed plasma. The narrowing of the distribution at the sheath edge is due to the fact that only the ions with velocities towards the object at $\Phi = 0$ V will enter the sheath.[28] The hump/tail at lower velocities is more pronounced for colder ions, as well as for larger potentials of the object Φ_s and heavier ions of the same temperature. We have verified that it is also present in the data considering total energy of the particles. Thus, some particles are not accelerated in the presheath to expected velocities and create a tail in the ivdf. We attribute this to electrostatic scattering of ions due to small local fluctuations of the potential in the sheath edge region. For faster ions, the scattering will be less pronounced, and the resulting distortion of the distribution at lower velocities will be smaller. We also note here that our definition of the sheath edge relates to the cold ion approximation. Since in our simulations ion temperatures are finite, our definition gives only approximate position of the sheath edge. Because of this and small potential fluctuations in the presheath, it is more appropriate to speak about the sheath edge region in this context.

Further inside the sheath, there will be less scattering as the ions are accelerated towards the object. The *fwhm* changes only little in the middle of the sheath, and here we get essentially distributions shifted towards higher velocities. The tail in the ivdf decreases, but is still present throughout the sheath, and contributes to an increase in the thermal velocity of the ivdf in the sheath.

Close to the surface, we observe an increase in *fhwm* for $\Phi_s = -95$ V and $\Phi_s = -40$ V, and we attribute it to a three dimensional dynamics of the ions in the sheath. Our simulated object is much larger than the Debye length, but when its potential is more negative than the floating potential, i.e., for large sheath, it can be addressed with the orbit-motion-limited theory.[29] Ions with large impact parameters, i.e., entering the sheath at large angles with respect to the direction towards the object, can have trajectories close to the surface that can lead to spreading in the radial direction. This energy spread close to the surface is also observed in the azimuthal velocity component close to the surface, as the orbiting ions stay longer in the sheath. Thus, the wings of the azimuthal ivdf get more pronounced further into the sheath, see again Fig. 1(c).

The development of the hump/tail in the ivdf in the presheath and sheath edge region in our simulations resembles the evolution of the ivdf in one-dimensional collisionless models with the plasma source.[8,9] In those models, the distribution in the sheath can often be divided into three parts, as there is different contribution of newly produced ions to the tail.[17] In our simulations, we do not have ionization, yet still in the presheath and sheath edge region, we observe a development of the tail/hump, which we attribute to the electrostatic scattering of ions. We observe the tail at the sheath edge and further inside the sheath. Similar tail has been observed for one-dimensional models with Maxwellian source function in the whole domain.[12] Note that similar distortions of the ivdf have been measured in different laboratory experiments.[18–20] The trend for different electron to ion temperature ratios in our simulations is similar to results from one-dimensional models.[12,13]

In many aspects the evolution of ivdf in our simulations resembles one-dimensional models, but this similarity is only apparent. A closer investigation of the ivdf shows discrepancies between our results for collisionless, source-free, three dimensional plasma and the Emmert model, see Fig. 2. In particular, the hump/tail in our results is present much further into the sheath, and close to the object surface, we observe a weak ion heating due to three-dimensional ion dynamics in the sheath. The contribution of the tail in the sheath leads to an increase of the thermal velocity, while the dominating part of the ivdf resembles a shifted distribution.

The changes (i.e., narrowing and development of hump/tail) in the ivdf in our simulations of stationary plasmas reflect the acceleration of the plasma towards the object so that the Bohm condition is satisfied. For supersonic flows, there is no significant changes in the ivdf in the sheath edge region, as ions already satisfy the Bohm condition, see again Fig. 5(a). For subsonic flows, ions are being accelerated, and a clear hump in the velocities develops at the sheath edge. Downstream from the object, the ivdfs are significantly widened in the presheath. This is due to the wake effects, where the ion focusing leads to a large spread in the ion velocities in the radial direction.[23,24] As the wake is more pronounced for supersonic velocities, the widening is also larger in this case. The broadening of the distribution on a downstream side is also consistent with kinetic Vlasov simulations for flowing plasmas.[30]

The shape in the radial ivdf close to the object surface for large δr, see again Fig. 1(a), is due to large spatial averaging in the direction normal to the surface in the region with a large velocity gradient. Such a broadening can be related to the spatial resolution in the LIF measurements and is important for the interpretation of such data.[12] In recent experiments,[20] the broadening of the ivdf was observed in the sheath where the potential drop was $\Delta\Phi = -100$ V with respect to the plasma potential, but not for the sheath where $\Delta\Phi = -50$ V, for which the velocity gradient was smaller. Also in other experiments, an increase in the ion temperatures normal to the sheath edge was observed.[19] These results are similar to those from our simulations for large δr. We suggest that one of the reasons for this broadening was superposed shifted ivdfs due to the spatial resolution in the measurement. However, for small δr, we still observe an increasing v_{th} around the sheath edge for $\Phi_s = -95$ V and $\Phi_s = -40$ V, which cannot be due to averaging. We note that another mechanism has also been proposed, which accounts for enhanced collisionality in the sheath due to ion acoustic instabilities.[6]

The spatial averaging can be equivalent to temporal averaging for the ivdf measured by the object with Φ_s varied in time. Recent measurements of the ivdfs in the RF sheath

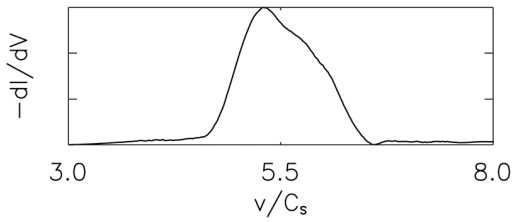

FIG. 6. Typical dI/dV from current to the RFEA measured in the experiment in the Njord device ($p \approx 0.03$ Pa, RF transmitter power 600 W, $B = 5$ mT). The current data was smoothed with the Savitzky-Golay filter before taking the derivative.

showed that large variations in velocities can occur within one RF cycle.[22,31–33] Thus, ion diagnostic tools in RF devices will be sensitive to RF-induced oscillations. An example is the retarded field energy analyzer (RFEA) located far away from the RF plasma source, as in the Njord device.[34–36] In Njord, the RF period $t_{RF} = 7.38 \times 10^{-8}$s, while the time t_s of an ion within a sheath of $10\lambda_{De}$ is of the order of 10^{-7} s. Thus, $t_s \approx t_{RF}$ placing the Njord experiment in the intermediate regime where RF contribution is strong enough to disturb the ivdf but too small to produce two distinct peaks.[33] A typical ivdf obtained from measurements with the RFEA in the Njord device is shown in Fig. 6. The shape of the distribution function from the RFEA does not agree with theoretical models for DC plasmas[16] but is similar to a radial ivdf for large δr, as shown in Fig. 1(a). We note that there will be yet another disturbance in the shape of the ion distribution function due to the opening angle.[37] Thus, a possible explanation of the shape of the ivdf from RFEA measurements shown in Fig. 6 can be that different ivdfs reach the aperture of the RFEA during integration time.

V. CONCLUSION

With three-dimensional particle-in-cell numerical simulations, we studied for the first time ion velocity distributions functions in the vicinity of a spherical object with a negative potential with respect to the plasma potential. It was demonstrated that for a source-free, collisionless plasma, a hump/tail forms in the radial ivdf in the presheath partly resembling one-dimensional analytical models. The broadening of the distribution due to three-dimensional ion dynamics closest to the surface has been observed both for stationary and flowing plasmas. The importance of the spatial and temporal resolutions in experimental measurements was also addressed.

ACKNOWLEDGMENTS

This work was supported by the Norwegian Research Council, NFR Grant No. 177570.

[1]J. E. Allen, Plasma Sources Sci. Technol. **18**, 014004 (2009).
[2]E. C. Whipple, Rep. Prog. Phys. **44**, 1197 (1981).
[3]D. Bohm, E. H. S. Burhop, and H. S. W. Massey, in *The Characteristics of Electrical Discharges in Magnetic Fields*, edited by A. Guthrie and R. K. Wakerling (McGraw-Hill, New York, 1949).
[4]E. R. Harrison and W. B. Thompson, Proc. Phys. Soc. London **74**, 145 (1959).
[5]J. E. Allen, J. Phys. D: Appl. Phys. **9**, 2331 (1976).
[6]S. D. Baalrud and C. C. Hegna, Plasma Sources Sci. Technol. **20**, 025013 (2011).
[7]M. A. Lieberman and A. J. Lichtenberg, *Principles of Plasma Discharges and Materials Processing* (John Whiley & Sons, Hoboken, 2005).
[8]G. A. Emmert, R. M. Wieland, A. T. Mense, and J. N. Davidson, Phys. Fluids **23**, 803 (1980).
[9]R. C. Bissell and P. C. Johnson, Phys. Fluids **30**, 779 (1987).
[10]R. J. Procassini, C. K. Birdsall, and E. C. Morse, Phys. Fluids B **2**, 3191 (1990).
[11]R. C. Bissell, P. C. Johnson, and P. C. Stangeby, Phys. Fluids B **1**, 1133 (1989).
[12]T. E. Sheridan, Phys. Plasmas **8**, 4240 (2001).
[13]S. Robertson, Phys. Plasmas **16**, 103503 (2009).
[14]L. A. Schwager and C. K. Birdsall, Phys. Fluids B **2**, 1057 (1990).
[15]A. Meige, O. Sutherland, H. B. Smith, and R. W. Boswell, Phys. Plasmas **14**, 032104 (2007).
[16]M. Sugawara and B. R. Stansfield, *Plasma Etching: Fundamentals and Applications* (Oxford University Press, Oxford, 1998).
[17]G. Bachet, L. Chérigier, and F. Doveil, Phys. Plasmas **2**, 1782 (1995).
[18]B. Jacobs, W. Gekelman, P. Pribyl, M. Barnes, and M. Kilgore, Appl. Phys. Lett. **91**, 161505 (2007).
[19]N. Sadeghi, M. van de Grift, D. Vender, G. M. W. Kroesen, and F. J. de Hoog, Appl. Phys. Lett. **70**, 835 (1997).
[20]N. Claire, G. Bachet, U. Stroth, and F. Doveil, Phys. Plasmas **13**, 062103 (2006).
[21]T. Lunt, G. Fussmann, and O. Waldmann, Phys. Rev. Lett. **100**, 175004 (2008).
[22]B. Jacobs, W. Gekelman, P. Pribyl, and M. Barnes, Phys. Rev. Lett. **105**, 075001 (2010).
[23]I. H. Hutchinson, Plasma Phys. Controlled Fusion **45**, 1477 (2003).
[24]W. J. Miloch, Plasma Phys. Controlled Fusion **52**, 124004 (2010).
[25]C. K. Birdsall and A. B. Langdon, *Plasma Physics via Computer Simulation* (Adam Hilger, New York, 1991).
[26]W. J. Miloch, M. Kroll, and D. Block, Phys. Plasmas **17**, 103703 (2010).
[27]J. Olson, W. J. Miloch, S. Ratynskaia, and V. Yaroshenko, Phys. Plasmas **17**, 102904 (2010).
[28]F. F. Chen, in *Plasma Diagnostic Techniques*, edited by R. H. Huddlestone and S. L. Leonard (Academic, New York, 1965).
[29]J. E. Allen, Phys. Scr. **45**, 497 (1992).
[30]F. Valsaque, G. Manfredi, J. P. Gunn, and E. Gautier, Phys. Plasmas **9**, 1806 (2002).
[31]U. Flender and K. Wiesemann, J. Phys. D: Appl. Phys. **27**, 509 (1994).
[32]N. Xiang and F. L. Waelbroeck, Phys. Plasmas **12**, 033505 (2005).
[33]D. Gahan, B. Dolinaj, and M. B. Hopkins, Rev. Sci. Instrum. **79**, 033502 (2008).
[34]H. S. Byhring, C. Charles, Å. Fredriksen, and R. W. Boswell, Phys. Plasmas **15**, 102113 (2008).
[35]Å. Fredriksen, L. N. Mishra, and H. S. Byhring, Plasma Sources Sci. Technol. **19**, 034009 (2010).
[36]Å. Fredriksen, L. N. Mishra, N. Gulbrandsen, and W. J. Miloch, J. Phys.: Conf. Ser. **257**, 012019 (2010).
[37]W. J. Miloch, N. Gulbrandsen, L. N. Mishra, and Å. Fredriksen, Appl. Phys. Lett. **97**, 261501 (2010).